



# Ce-substituted $\text{LaNiO}_3$ mixed oxides as catalyst precursors for glycerol steam reforming



Carlos A. Franchini<sup>a</sup>, Wladimir Aranzuez<sup>b</sup>, Andréa M. Duarte de Farias<sup>a</sup>, Gina Pecchi<sup>b,\*\*</sup>, Marco A. Fraga<sup>a,\*</sup>

<sup>a</sup> Instituto Nacional de Tecnologia/MCTI, Laboratório de Catálise, Av. Venezuela, 82/518, 20081-312 Rio de Janeiro/RJ, Brazil

<sup>b</sup> Universidad de Concepción, Casilla 160-C, Concepción, Chile

## ARTICLE INFO

### Article history:

Received 17 May 2013

Received in revised form 26 July 2013

Accepted 23 August 2013

Available online 31 August 2013

### Keywords:

Hydrogen production

Nickel catalyst

Deactivation

Carbon deposition

## ABSTRACT

Mixed oxides of general formula  $\text{La}_{1-x}\text{Ce}_x\text{NiO}_3$  were prepared by self-combustion method and taken as precursors of Ni-supported catalysts for an experimental investigation of steam reforming of glycerol. The mixed oxide precursors and the corresponding derived fresh catalysts were characterized by XRD, TPR and TEM while the used catalysts were investigated by FE-SEM, TEM and TPO/TGA-MS. All catalysts were investigated on glycerol steam reforming with special focus on the resistance to deactivation. The precursors led to active catalysts, producing hydrogen-rich gas stream. Deactivation was seen to occur irrespective of catalyst composition. Substitution of 50% La by Ce provided more deactivation-resistant catalyst, allowing only minor amount of more reactive carbon deposits. It was suggested to be associated with the formation of  $\text{CeO}_2\text{--La}_2\text{O}_3$  solid solutions, as evidenced by XRD, which would act as an oxygen buffer and therefore facilitate the removal of carbon deposits onto the catalyst surface.

© 2013 Elsevier B.V. All rights reserved.

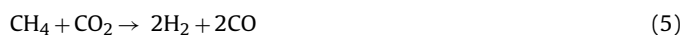
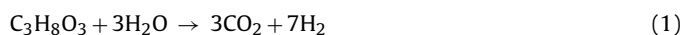
## 1. Introduction

Hydrogen production has been extensively studied over the last years as it is a carbon-free energy carrier and thus its use in fuel cells would generate no harmful emissions during power generation. Much progress has been achieved so far on the development of reforming processes, particularly those based on fossil feedstocks as natural gas and coal [1]. Meanwhile, an environmentally friendly and clean energy production relying on hydrogen may only be established whether it is generated from a carbon-free source or a carbon neutral process. Renewable feedstocks are thus highly interesting as hydrogen source and many efforts have indeed been done to establish an economical, efficient green reforming process [2,3].

Glycerol stands out in this scenario as its availability has been steadily growing due to the demand of biofuels worldwide. Produced from vegetable oils, which are triglycerides, transesterified biodiesel leads to a significant amount of glycerol sidestream. Generating hydrogen from this valuable biomass feedstock would provide an additional energy supply intensifying the biofuel production. Moreover, this non-toxic biomass has quite safe storage and handling policies. Such an integrated bioenergy production

model may indeed allow a sustainable environmental local development.

Aqueous phase (APR) [4–7] and steam reforming (SR) [8–11] reactions have been increasingly studied to generate hydrogen from glycerol. Whilst APR requires high pressures, which may decrease the selectivity to hydrogen, glycerol SR is thermodynamically favoured at low pressures and can be performed at atmospheric conditions. Furthermore this latter route is endothermic ( $\Delta H_{298}^0 = +123 \text{ kJ mol}^{-1}$ ) and thus a high-temperature operation is required to increase hydrogen yield [12]. However, one should bear in mind that glycerol SR is a quite complex process since a wide variety of reactions may take place. Whereas the overall process can be represented by Eq. (1), which is the result of simultaneous glycerol decomposition (Eq. (2)) and water-gas shift (Eq. (3)) reactions, methanation (Eq. (4)), methane dry reforming (Eq. (5)) and a series of reaction for carbon formation (Eqs. (6)–(9)) may also take place depending on the operation conditions.



\* Corresponding author. Tel.: +55 2121231152; fax: +55 2121231051.

\*\* Corresponding author.

E-mail addresses: [gpecchi@udec.cl](mailto:gpecchi@udec.cl) (G. Pecchi), [marco.fraga@int.gov.br](mailto:marco.fraga@int.gov.br), [fraga.marco@yahoo.com.br](mailto:fraga.marco@yahoo.com.br) (M.A. Fraga).



Besides reaction conditions, the catalyst also plays a key role on determining the reaction pathway and product distribution. It is a consequence of the fundamental steps involving the cleavage of C–C, O–H and C–H bonds of glycerol molecule while keeping the C–O ones. As a result, a growing number of papers reporting the performance of different catalytic systems for this SR process has been published over recent years. Even though heterogeneous catalysts based on supported noble metals, mainly Pt [13,14], Ru [15], Rh [16,17] and Ir [18], have been reported for glycerol SR, Ni-based systems stand as the most investigated ones so far. As a matter of fact, Ni is a less costly alternative and is well known to promote the rupture of C–C bonds. On the other hand, this transition non-noble metal presents a high carbon formation rate, which invariably leads to a dramatic catalyst deactivation on hydrocarbon and alcohol reforming processes.

In an attempt to overcome such major drawback, some effort has been done to design and develop more suitable Ni-based catalysts. Different oxides have been employed in the preparation of supported Ni systems, such as  $\text{Al}_2\text{O}_3$ ,  $\text{SiO}_2$ ,  $\text{MgO}$ ,  $\text{TiO}_2$ ,  $\text{CeO}_2$ ,  $\text{ZrO}_2$  and  $\text{CeO}_2\text{–ZrO}_2$ . It has been consistently observed that supports featuring a more basic character provide more active and deactivation-resistant catalysts [7,19,20]. Alternative approaches such as combining Ni with promoters, particularly Sn and La, have also shown to be effective to enhance catalytic activity [21–23]. In some cases, however, an adequate balance between metal and acid/base sites is claimed to be responsible for hydrogen production [20,23,24]. Hence it should be also considered the contribution of the support and catalyst synthesis method to suppress the carbon formation in the reforming process by controlling nickel dispersion. Indeed the significant influence of nickel particle size on the nucleation rate of carbon has been usually reported for both methane and ethanol reforming [25,26]; the initiation step for carbon formation being more difficult for smaller particle sizes [26]. Nevertheless, no clear evidence has been published so far concerning glycerol SR.

From this literature background, the importance of catalyst architecture is clear. A suitable surface should ideally present a well-balanced distribution of metal nanoparticles and basic and redox centres. Synthesizing such a system is quite challenging though, particularly if conventional synthesis procedures of metal-supported catalysts are considered.

The use of perovskite-type mixed oxides, represented by the general formula  $\text{ABO}_3$ , as catalyst precursor is certainly a promising approach and deserves more attention. In  $\text{ABO}_3$  structures, A-site is a large rare earth cation and B-site is a small cation of a d-transition metal, which may be partially substituted by A' and B' cations of similar oxidation state and ionic radius. After reducing the B-site cations, well-dispersed B metal nanoparticles supported on a stable A oxide support will be obtained. A large number of papers with a wide-ranging type of A and B cations in the perovskite structure with different degrees of substitution has indeed evidenced the highly dispersed state of the metal phase on the final supported catalyst [27–30]. Furthermore the enhanced catalytic performance of perovskite-derived catalysts on methane [28,31,32] and ethanol [33,34] reforming is also quite motivating. As a matter of fact, a recent contribution by Cui et al. [12] compared the activity of  $\text{La}_{1-x}\text{Ce}_x\text{NiO}_3$  catalyst to the thermodynamic equilibrium of glycerol SR. It was reported that Ce substitution in the perovskite structure improved the catalytic conversion approaching to the

equilibrium under certain operation conditions. It was also briefly stated that the catalysts were stable on time on stream [12].

Here, mixed oxides of general formula  $\text{La}_{1-x}\text{Ce}_x\text{NiO}_3$  were taken as precursors of Ni-supported catalysts for an experimental investigation of steam reforming of glycerol. Different degrees of lanthanum substitution by cerium cations were evaluated as regarding catalytic activity and resistance to deactivation aiming at contributing to the scarce discussion of carbon formation when processing glycerol to generate green hydrogen.

## 2. Experimental

### 2.1. Synthesis of mixed oxides

Partially substituted  $\text{La}_{1-x}\text{Ce}_x\text{NiO}_3$  ( $x = 0.0, 0.1, 0.3, 0.5, 0.7$  and  $0.9$ ) mixed oxides were prepared by the self-combustion method [35]. Glycine ( $\text{H}_2\text{NCH}_2\text{CO}_2\text{H}$ ), used as ignition promoter, was added to an aqueous solution of metal nitrates with the appropriate stoichiometry in order to get a  $\text{NO}_3^-/\text{NH}_2$  (molar ratio) = 1. The resulting solution was slowly evaporated until a vitreous green gel was obtained. The gel was heated up to around  $250^\circ\text{C}$ , temperature at which the ignition reaction occurs producing a powdered precursor, which still contains carbon residues. The solids were crushed and sieved to obtain the required particle size ( $<200\text{ }\mu\text{m}$ ) prior to calcination at  $700^\circ\text{C}$  in air for 10 h to eliminate all of the remaining carbon. Hereinafter, the samples will be simply designated by the amount of Ce, i.e.,  $x = 0, x = 0.1, x = 0.3, x = 0.5, x = 0.7$  and  $x = 0.9$ .

### 2.2. X-ray diffraction of synthesized mixed oxides

Powder X-ray powder diffraction (XRD) patterns were obtained with nickel-filtered  $\text{Cu K}\alpha_1$  radiation ( $\lambda = 1.5418\text{ \AA}$ ), using a Rigaku diffractometer. The measurements were carried out with  $2\theta$  ranging from  $10^\circ$  to  $70^\circ$ , with a scanning rate of  $0.01^\circ\text{ s}^{-1}$ .

### 2.3. Temperature-programmed reduction of synthesized mixed oxides

Temperature-programmed reduction (TPR) experiments were performed in a TPR/TPD 2900 Micromeritics system with a thermal conductivity detector (TCD). TPR profiles were collected up to  $700^\circ\text{C}$  following a  $10^\circ\text{C min}^{-1}$  linear temperature ramp and using a 5%  $\text{H}_2/\text{Ar}$  (vol.%) stream as the reducing gas ( $30\text{ mL min}^{-1}$ ).

### 2.4. Characterization of fresh reduced catalysts – X-ray diffraction and transmission electron microscopy

The catalysts derived from mixed oxides precursors were examined by powder XRD and transmission electron microscopy (TEM). Prior to analysis, the solids were reduced under pure hydrogen flow ( $50\text{ mL min}^{-1}$ ) at  $700^\circ\text{C}$  for 2 h. After, the reactor was purged with nitrogen and cooled down to room temperature. It was then placed in a cryostatic bath and a flow of 5%  $\text{O}_2/\text{Ar}$  was admitted into the reactor for 1 h. Afterwards, it was purged for 30 min with nitrogen under the same cryostatic conditions and finally the bath was removed and the catalyst bed was allowed to stabilize at room temperature. The passivated samples were ultrasonically suspended in isopropanol and deposited on a carbon-coated copper grid for TEM examination using a Tecnai 20 FEI microscope operating at 200 kV. All size measurements were processed using Axio Vision software version 4. XRD analyses were performed using the same experimental conditions described hereinbefore.

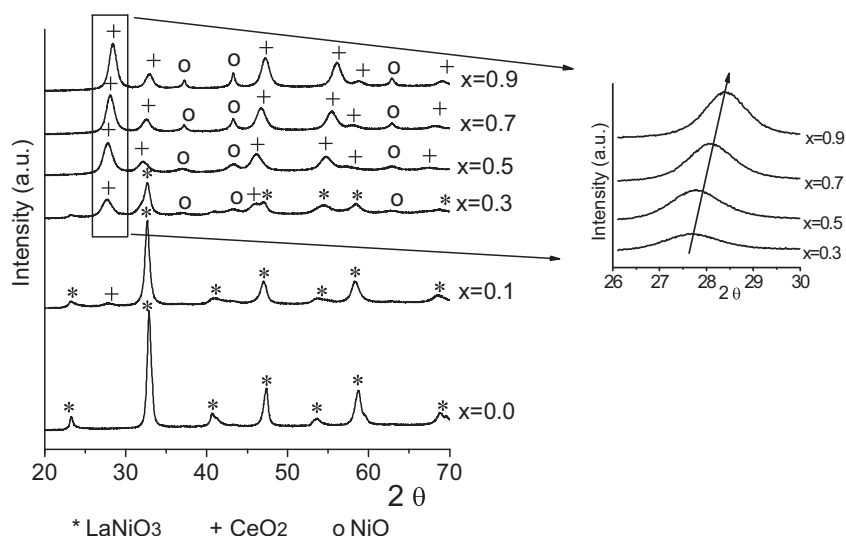


Fig. 1. XRD patterns of calcined  $\text{La}_{1-x}\text{Ce}_x\text{NiO}_3$  samples.

### 2.5. Catalytic activity

Catalytic activity and stability were evaluated on steam reforming of glycerol in a commercial Microactivity Reference apparatus from PID Eng&Tech using a fixed-bed tubular reactor. In a typical test, 100 mg of powdered catalyst was diluted with SiC up to a catalytic volume of 0.6 mL. Prior to the reaction, the catalysts were reduced in situ at 700 °C for 1 h under pure hydrogen. Afterwards, the reactor system was purged with nitrogen and cooled down to the reaction temperature. An HPLC pump was used to feed the reactor with a glycerol solution (30 wt.%) at 0.32 mL min<sup>-1</sup>. This feed stream was diluted with a 50 mL min<sup>-1</sup> flow of nitrogen. All tests were monitored for 6 h and the gas composition was determined by an on-line HP 6890A gas chromatograph with TCD/FID detectors. The concentration of unreacted glycerol in the liquid phase was analyzed by a Waters Alliance HPLC with an Aminex HPX 87H column, using 0.05 mol L<sup>-1</sup> H<sub>2</sub>SO<sub>4</sub> as eluent at 0.7 mL min<sup>-1</sup> and a refractive index detector (RID).

Global conversion of glycerol ( $X_{\text{global}}$ ) was calculated based on glycerol concentration:

$$X_{\text{global}} = \frac{F_{\text{gly}}^{\text{in}} - F_{\text{gly}}^{\text{out}}}{F_{\text{gly}}^{\text{in}}} \times 100$$

Glycerol conversion to gaseous products ( $X_{\text{gas}}$ ) was determined from the molar flow of the non-condensable products in the outlet ( $F$ ) and the glycerol molar flow in the inlet:

$$X_{\text{gas}} = \frac{F_{\text{CH}_4} + 2F_{\text{C}_2\text{H}_6} + 2F_{\text{C}_2\text{H}_4} + F_{\text{CO}_2} + F_{\text{CO}}}{3F_{\text{gly}}^{\text{in}}} \times 100$$

The molar composition in the gaseous stream was determined from:

$$S_i = \frac{C_i}{\sum C_i} \times 100$$

where  $C_i$  is the concentration of product  $i$ .

### 2.6. Characterization of used catalysts – temperature-programmed oxidation, field emission scanning electron microscopy and transmission electron microscopy

The used catalysts were collected after 6-h reaction and characterized in order to infer on the deactivation process.

Temperature-programmed oxidation was performed in a TA Instruments SDT Q600 thermobalance coupled with an Ametek quadrupole mass spectrometer (TPO/TGA-MS). The analyses were conducted following a heating rate of 20 °C min<sup>-1</sup> up to 900 °C under synthetic air at 50 mL min<sup>-1</sup>. These samples were also examined by field emission scanning electron microscopy (FE-SEM) on a Quanta 200 FEI microscope operating with an accelerating voltage of 20 kV. Finally, the used catalysts were ultrasonically suspended in isopropanol and deposited on a carbon-coated copper grid for TEM examination using a Tecnai 20 FEI microscope.

## 3. Results and discussion

### 3.1. X-ray diffraction of synthesized mixed oxides

The XRD patterns of the as-synthesized  $\text{La}_{1-x}\text{Ce}_x\text{NiO}_3$  samples are shown in Fig. 1. The diffraction patterns of unsubstituted  $\text{LaNiO}_3$  correspond to a perovskite with a rhombohedral (JC-PDF 330711) structure [36] and no other crystalline phase was detected whatsoever. When La is partially substituted by Ce at low concentration ( $x=0.1$ ), a similar XRD pattern is registered; the diffraction line at  $2\theta = 32.7^\circ$  corresponding to  $\text{LaNiO}_3$  structure decreases in intensity but no significant distortion in the perovskite structure is promoted. By increasing the amount of Ce in the composition, the patterns change more significantly; the typical perovskite diffraction lines are still detected along with new peaks associated with an isolated  $\text{CeO}_2$  phase at  $x=0.3$ . At higher Ce loadings, however, the formation of a perovskite structure could no more be stated and only  $\text{CeO}_2$  and  $\text{NiO}$  crystalline phases were identified. None of the diffractions associated with lanthana appeared in the XRD patterns, indicating that it did not form any crystalline phase distinct from ceria or  $\text{NiO}$ .

The diffractions ascribed to the (111), (200), (220), (311) and (222) planes of a face-centred cubic (fcc) fluorite  $\text{CeO}_2$  structure are present in the patterns of all solids with  $x > 0.3$  and become more defined and intense as the Ce content in the solid composition increases. Nevertheless it can be noted that the diffractions associated with the fcc fluorite structure clearly shift towards higher Bragg angles along with the increase in Ce loading (Fig. 1, inset). This fashion indicates different degrees of distortion of ceria crystal lattice as a consequence of the insertion of larger  $\text{La}^{3+}$  (1.17 Å) into  $\text{CeO}_2$  structure ( $\text{Ce}^{4+} = 0.97$  Å). Indeed the higher the content of

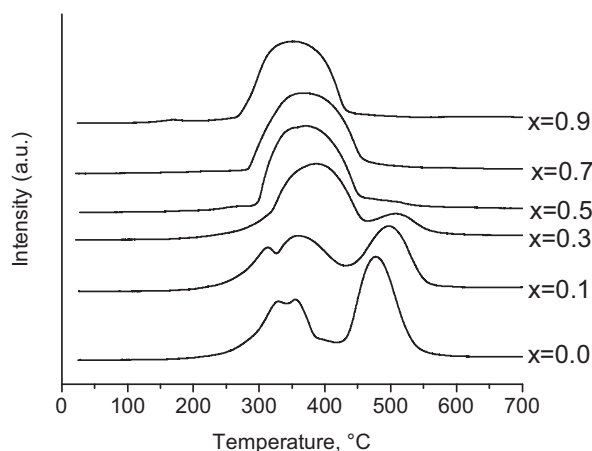


Fig. 2. TPR profiles of calcined  $\text{La}_{1-x}\text{Ce}_x\text{NiO}_3$  samples.

La, the more expanded the crystal lattice and the lower the Bragg angle the fcc fluorite diffractions shift to.

The unit-cell lengths  $a$  of these La-Ce structures calculated from the (1 1 1) reflection are summarized in Table 1. Considering the cell length of 0.539 nm usually reported for pure  $\text{CeO}_2$  powders [37,38], the values found for the samples in this work consistently increases with the lanthana-doping level, indicating the lattice expansion caused by the enrichment of ceria-based cubic structure with lanthana.

The average crystallite diameter  $d_{hkl}$  of the lanthana-doped ceria samples was also estimated from the peak (1 1 1) using the Scherrer equation [39,40] and the data are also collected in Table 1. It is noted that replacement of  $\text{Ce}^{4+}$  with larger  $\text{La}^{3+}$  in the  $\text{CeO}_2$  lattice remarkably affected the mean particle diameter, being smaller as the lanthanum content increases. It should be mentioned that similar trend has already been found by other groups when doping ceria with other lanthanides [37,38,40].

As for  $\text{NiO}$ , the diffractions related to the (1 1 1), (2 0 0) and (2 2 0) planes appearing at  $37.2^\circ$ ,  $43.3^\circ$  and  $62.9^\circ$  ( $2\theta$ ), respectively, are more clearly seen from  $x = 0.5$  (Fig. 1). These peaks grow in intensity upon increasing ceria loading because excessive amount of foreign cation causes oxides to segregate. Additionally, no structural deformation may be envisaged by XRD.

### 3.2. Temperature-programmed reduction of synthesized mixed oxides

The reduction behaviour of  $\text{La}_{1-x}\text{Ce}_x\text{NiO}_3$  samples was investigated by ordinary temperature-programmed reduction analysis ( $\text{H}_2$ -TPR<sub>1</sub>) and the results are presented in Fig. 2.

The hydrogen consumption profile of  $\text{LaNiO}_3$  structure ( $x = 0$ ) shows two unresolved reduction events within 300–400 °C that correspond to the partial reduction of perovskite network. The first reduction step is related to the formation of  $\text{La}_4\text{Ni}_3\text{O}_{10}$  [41], whose reduction occurs subsequently leading to the formation of the intermediate oxygen-deficient  $\text{La}_2\text{NiO}_4$  perovskite phase [41–43]. A third reduction peak is also registered at higher temperature ( $\sim 470^\circ\text{C}$ ) and corresponds to the complete reduction of  $\text{Ni}^{2+}$  from the  $\text{La}_2\text{NiO}_4$  perovskite to yield  $\text{La}_2\text{O}_3$ ,  $\text{CeO}_2$  and  $\text{Ni}^0$  metallic nanoparticles [41].

Upon La partial substitution, the  $x = 0.1$  and 0.3 samples show roughly the same behaviour of  $\text{LaNiO}_3$  perovskite being the reduction processes similarly described. However, the first two steps associated with the reduction of  $\text{Ni}^{3+}$  ions of  $\text{LaNiO}_3$  to  $\text{La}_2\text{NiO}_4$  are more or less merged according to the composition. It is also notorious that the intensity of the first reduction steps are more

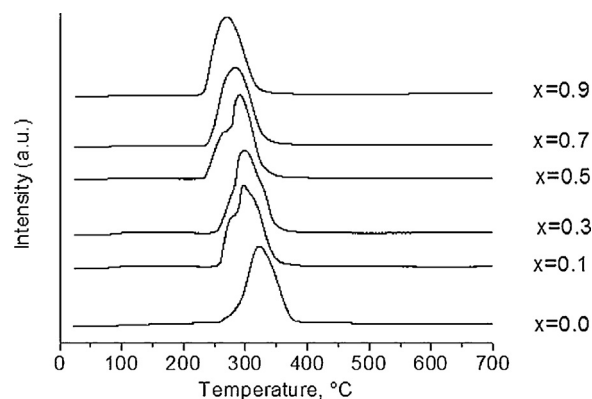


Fig. 3. Profiles of the second TPR cycle of  $\text{La}_{1-x}\text{Ce}_x\text{NiO}_3$  samples.

significant while the third reduction stage is much less pronounced for  $\text{La}_{0.7}\text{Ce}_{0.3}\text{NiO}_3$  ( $x = 0.3$ ). These findings are consistent with the minor presence of the perovskite structure in this sample and the existence of other segregated oxide phases as evidenced by XRD analysis (Fig. 1). As a consequence, besides the previously described stepped reduction of  $\text{LaNiO}_3$  ( $x = 0$ ), other reduction processes may take place, such as  $\text{Ni}^{2+}$  from  $\text{NiO}$  segregated phase, overlapping in the same temperature range. Similar patterns have been reported by other groups [32,34].

On the other hand, for higher substitution levels ( $x \geq 0.5$ ) the profiles consist of only one asymmetrical and broad reduction peak, which may be assigned to the reduction of  $\text{NiO}$ . An eventual partial reduction of ceria-based oxides may not be ruled out at this point though.

Further evidences were collected from second temperature-programmed reduction cycles ( $\text{H}_2$ -TPR<sub>2</sub>). This procedure consisted of cooling down the samples to room temperature after switching the  $\text{H}_2/\text{Ar}$  flow to pure Ar at the end of the first TPR analysis. The solids were then oxidized under  $\text{O}_2/\text{He}$  stream up to 700 °C and finally the second reduction profiles were collected (TPR<sub>2</sub>) once the sample was cooled back to room temperature. Since no samples would present a perovskite structure any longer due to the structural collapse upon the first reduction cycle,  $\text{NiO}$  dispersed on lanthanide oxides ( $\text{CeO}_2$ ,  $\text{CeO}_2\text{-La}_2\text{O}_3$  and/or  $\text{La}_2\text{O}_3$ ) should be expected instead and similar  $\text{NiO}$  reduction profile could be foreseen for all TPR<sub>2</sub> analyses. Moreover, a more reliable quantitative analysis may be done since it is carried out in situ immediately after the first reduction/oxidation cycle. The results featured in Fig. 3 and Table 1 are indeed in close agreement with such prediction. All TPR<sub>2</sub> profiles show only one reduction peak that corresponds to the typical reduction of  $\text{NiO}$  dispersed on metal oxides and presented practically the same hydrogen uptake. Those values are higher than the theoretical one, suggesting that other oxides entities are being reduced as well.

### 3.3. Characterization of fresh reduced catalysts – XRD and TEM

According to TPR results, these Ce-substituted  $\text{LaNiO}_3$  mixed oxides were reduced at 700 °C, temperature at which all nickel oxides could be reduced, before glycerol steam reforming. The reduced samples were initially investigated by XRD and transmission electron microscopy (TEM). As expected, the diffraction patterns of the reduced samples changed completely from those previously recorded for the calcined solids (Fig. 4).

Complete loss of the perovskite structure is seen for Ni-containing solids with  $x \leq 0.3$  as the most intense diffraction line

**Table 1**

CeO<sub>2</sub> lattice cell length ( $a_{\text{CeO}_2}$ ), CeO<sub>2</sub> crystallite mean particle size ( $d_{\text{hkl}}\text{CeO}_2$ ), metallic Ni crystallite mean particle size ( $d_{\text{hkl}}\text{Ni}$ ), hydrogen uptake and amount of carbon deposited on the used catalysts (gC/g<sub>cat</sub>).

Sample	$a_{\text{CeO}_2}$ (nm)	$d_{\text{hkl}}\text{CeO}_2$ (nm)	$d_{\text{hkl}}\text{Ni}$ (nm)	H <sub>2</sub> uptake <sup>a</sup> (mmol/g)	gC/g <sub>cat</sub>
$x=0$	–	–	9.4	6.1	0.23
$x=0.1$	–	–	6.6	6.0	0.16
$x=0.3$	0.558	6.2	8.4	5.8	–
$x=0.5$	0.555	7.3	7.5	5.8	0.03
$x=0.7$	0.550	8.4	14.1	5.7	0.07
$x=0.9$	0.544	19.5	16.3	5.5	–

<sup>a</sup> Theoretical hydrogen uptake for sample reduction = 4.1 mmol/g (as calculated by assuming that NiO is stoichiometrically reduced to Ni<sup>0</sup>).

of such phase at  $2\theta = 32.7^\circ$  fully disappears. In contrast new peaks assigned to La(OH)<sub>3</sub> and metallic Ni<sup>0</sup> phases are now noted for both  $x=0$  and  $x=0.1$  reduced samples along with tiny diffractions that may be ascribed to the oxygen-deficient La<sub>2</sub>NiO<sub>4</sub> perovskite. From  $x=0.3$ , fcc fluorite distorted CeO<sub>2</sub> structure and Ni<sup>0</sup> are the only crystalline phases identified. The unit cell lengths  $a$  is once again found to shift to lower Bragg angles for the catalysts with higher loadings of lanthanum, indicating that the CeO<sub>2</sub>–La<sub>2</sub>O<sub>3</sub> solid solutions are kept upon reduction.

It should be noted that diffraction lines at  $2\theta = 44.4^\circ$  and  $52^\circ$ , corresponding to metallic nickel, could be distinguished for all samples and the broad peaks suggest the presence of Ni<sup>0</sup> in a high dispersion degree in agreement with what has been found by other groups when using perovskite type mixed oxides as catalyst precursor [44]. The average Ni particle sizes estimated by using Scherrer equation using the diffraction at  $44.4^\circ$  is shown in Table 1. It is seen that the extension of La substitution influences the size of Ni nanoparticles, which steadily decreases up to  $x=0.5$  and then steeply increases at higher Ce content. A similar trend has been previously reported by de Lima et al. [34].

Ni nanoparticles were further examined by TEM and some representative images are displayed in Fig. 5. Ni<sup>0</sup> domains as small as 7 nm could often be found in close agreement with the average size estimated by the XRD patterns of  $x \leq 0.5$  samples (Table 1). Nevertheless, it should be pointed out that smaller particles (~5 nm) along with much larger domains (20–25 nm) were also eventually observed for all samples.

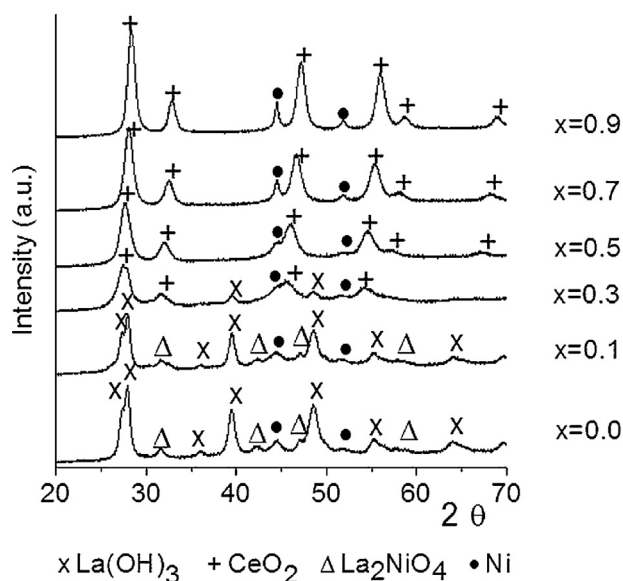


**Fig. 4.** XRD patterns of reduced metal supported catalysts derived from La<sub>1-x</sub>Ce<sub>x</sub>NiO<sub>3</sub>.

### 3.4. Catalytic activity

Glycerol steam reforming was firstly evaluated over LaNiO<sub>3</sub> perovskite-derived catalyst ( $x=0$ ) at different temperatures and the reaction was conducted for 6 h in order to assess catalytic activity and stability. Initial global glycerol conversions (after 1-h reaction) at 500 °C and 700 °C are presented in Fig. 6a. As expected, glycerol conversion ( $X_{\text{global}}$ ) gradually increases along with reaction temperature. Blank experiments without any catalyst were carried out before catalyst evaluation and showed that under the used conditions glycerol conversion also occurs homogeneously at gas phase, being considerably significant at 700 °C, reaching 88% (Fig. 6a). Studies at such a high temperature should thus be avoided to afford inferring on the catalyst performance and deactivation resistance.

Hydrogen and CO<sub>2</sub> were the major products formed with selectivities at around 70% and 25%, respectively, at all reaction temperatures; CO and small amounts of hydrocarbons (methane and ethylene) could also be detected (Fig. 6b).

Based on these performances, the catalysts derived from Ce-substituted LaNiO<sub>3</sub> mixed oxides were tested and compared at 500 °C in order to minimize the contribution from homogeneous reaction. This reaction conditions would also facilitate the eventual formation of carbon deposits, allowing the investigation of any benefit from Ce addition to stability.

Fig. 7 contrasts the catalytic performance of samples under the same conditions. Notwithstanding the catalyst features or degree of La substitution by Ce, a drop in global conversion on time on stream could always be seen. However, the sample derived from the mixed oxide with an equivalent content of La<sup>3+</sup> and Ce<sup>3+</sup> ( $x=0.5$ ) was found to be much more stable with a promising behaviour, which may be associated with the formation of a CeO<sub>2</sub>–La<sub>2</sub>O<sub>3</sub> solid solution as suggested by XRD results. Moreover, overall activity seems not to be affected by Ni particle size since no clear correlation could be envisaged with the data collected from XRD and TEM analyses.

On the other hand, catalysts with Ce loadings above and below 50% led to a dramatic decrease in glycerol global conversion, revealing a strong deactivation process; indeed  $x=0.1$  and  $x=0.7$  samples presented conversions within 5–20% right after the first hour.

Despite the clear deactivation process, the distribution of products in the gas phase and the catalyst gaseous conversions ( $X_{\text{gas}}$ ) were quite stable and minimal variations could be observed upon differences in the composition of the catalysts. H<sub>2</sub> and CO<sub>2</sub> were always the main gas products and the selectivities are summarized in Table 2. The H<sub>2</sub>/CO<sub>2</sub> ratios suggest that the main process occurring is indeed glycerol steam reforming (Eq. (1)), since the experimental values are reasonably close to the theoretical 2.3.

The low conversion to gaseous products ( $X_{\text{gas}}$ ) is a consequence of the reaction temperature, particularly considering the endothermic nature of the overall steam reforming reaction. In this sense, glycerol conversion to gaseous products ( $X_{\text{gas}}$ ) increases by increasing the temperature [12]. Conversely, glycerol conversion to some liquid products through different reaction routes (as for example, glycerol hydrogenolysis) is expected to increase at low temperatures due to the exothermic character of such reactions. Indeed,

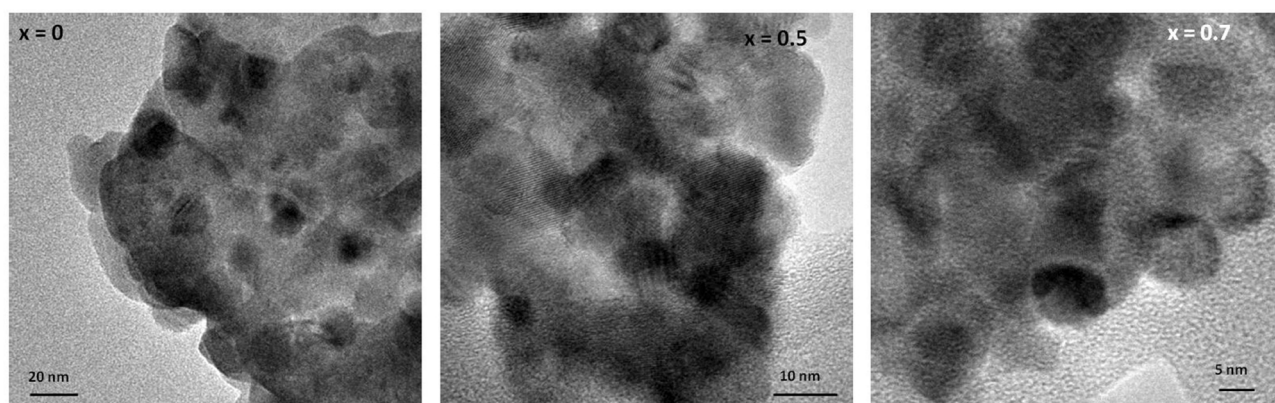


Fig. 5. Representative TEM images of some reduced metal supported catalysts derived from  $\text{La}_{1-x}\text{Ce}_x\text{NiO}_3$ .

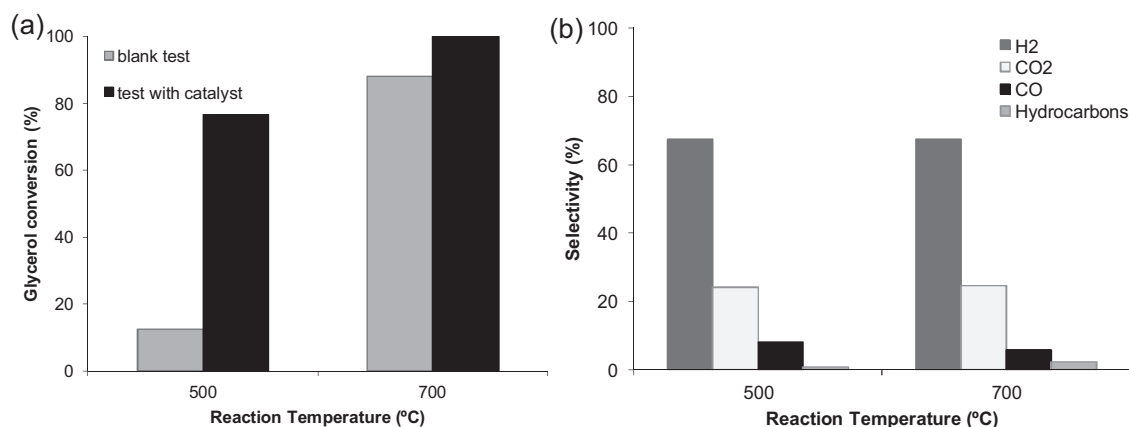


Fig. 6. Glycerol conversion (a) and product selectivity (b) of reactions without (blank) and with catalyst at 500 °C and 700 °C.

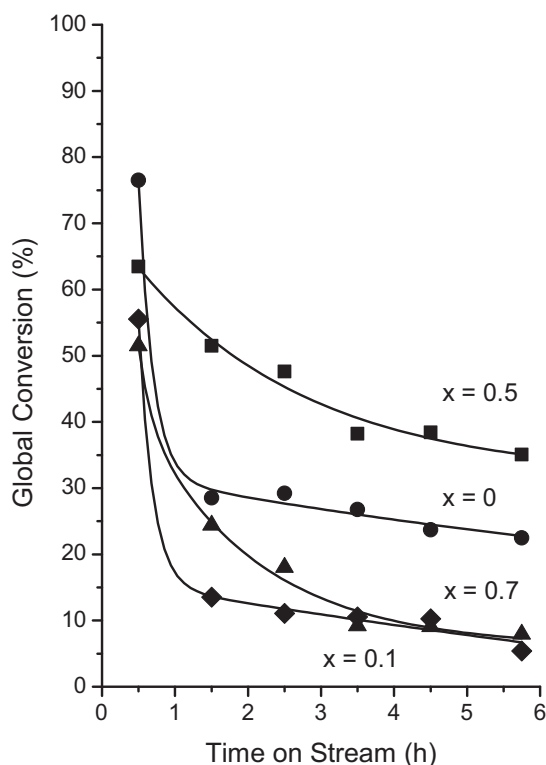


Fig. 7. Evolution of global glycerol conversion as a function of time on stream for glycerol steam reforming at 500 °C over all mixed oxide-derived catalysts.

Table 2

Conversion to gaseous products ( $X_{\text{gas}}$ ) and product selectivity obtained over all metal supported catalysts derived from  $\text{La}_{1-x}\text{Ce}_x\text{NiO}_3$ .

Sample	$X_{\text{gas}}$ (%)	Selectivity (mol%)			
		H <sub>2</sub>	CO <sub>2</sub>	CO	Hydrocarbons <sup>a</sup>
$x = 0$	16	69	25	6	–
$x = 0.1$	14	71	24	3	2
$x = 0.5$	16	69	25	5	1
$x = 0.7$	13	75	18	5	2

<sup>a</sup> Hydrocarbons = methane and ethylene.

the values accomplished for the catalysts presented herein (Table 2) are in very good agreement with the expected ones as presented elsewhere [45] considering the operation conditions, especially the reaction temperature (500 °C), which is quite low for complete conversion to gaseous products.

The deactivation process observed for the catalysts reported in this work differs from those only briefly reported elsewhere over similar systems [12]. Such differences may rely on the distinct operation conditions, particularly the space velocity and the concentration of glycerol in the feed stream. Indeed the influence of glycerol concentration has been claimed to be extremely relevant to catalyst activity and stability [46].

### 3.5. Characterization of used catalysts – FE-SEM, TEM and TPO/TGA-MS

To investigate the causes of the deactivation process undergone by all samples, FE-SEM analyses were conducted. The FE-SEM

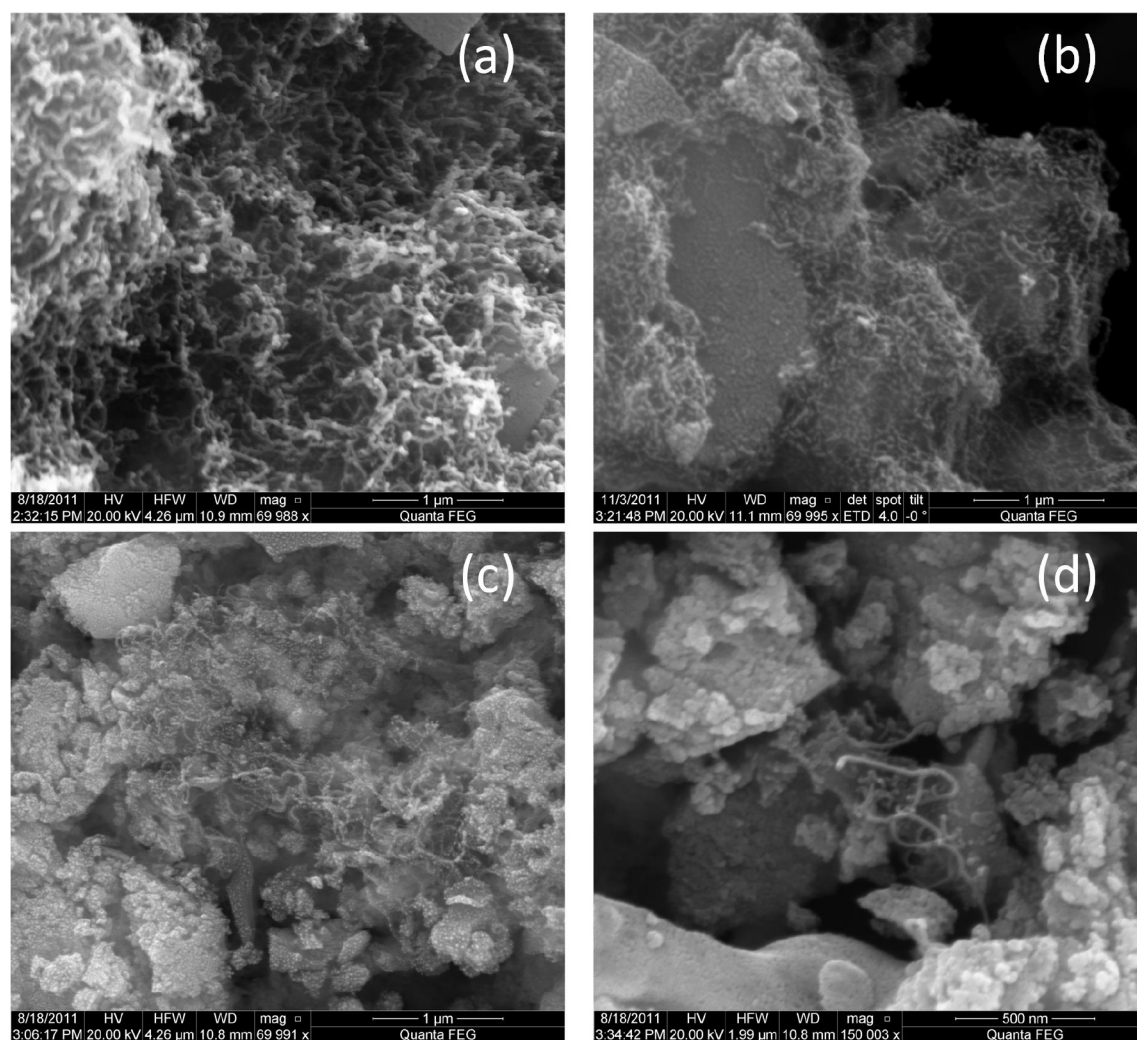


**Fig. 8.** Representative FE-SEM images of some metal supported catalysts derived from  $\text{La}_{1-x}\text{Ce}_x\text{NiO}_3$  after glycerol steam reforming: (a)  $x=0$ , (b)  $x=0.1$ , (c)  $x=0.5$  and (d)  $x=0.5$  at higher magnification ( $150,000\times$ ).

images revealed that the deactivation of unsubstituted  $\text{LaNiO}_3$  perovskite-derived catalyst ( $x=0$ ) is due to the formation of filamentous carbon. Consistently, they were easily and plentifully found on this sample (Fig. 8a). The formation of carbon nanostructures, however, did not happen equally over all Ce-containing catalysts. Catalysts with low and high Ce loadings also presented considerable amounts of carbon filaments and similar FE-SEM images were collected (Fig. 8b). Conversely, only after a much more detailed and meticulous analysis few filaments could be found over  $x=0.5$  solid (Fig. 8c and d).

Studies on carbon deposition over Ni-based catalysts have been extensively reported and the mechanism of coke formation is rather well established for steam reforming of methane [2,47,48] and ethanol [3,49,50]. As regarding glycerol steam reforming, a systematic mechanistic investigation is still missing. However, some recent contributions [20,24,46,51,52] have reported the deactivation of Ni-supported catalysts on SR of glycerol and associated this phenomenon with the formation of both highly reactive carbon species and low reactive more ordered structures particularly filamentous carbon. Unlike what is observed for methane SR, sintering of the active Ni phase is claimed to have no relevant contribution when glycerol is used as feedstock. On the other hand, the catalyst morphology has revealed to strongly influence deactivation and structured catalysts (monolith) have indeed shown to be more

deactivation-resistant than conventional powder or pellet systems [52]. It has been claimed to be a consequence of the strong interaction between the catalyst nanoparticles and the alumina layer in the monolith [52].

As it has been highlighted by many authors [20,24,46,51,52], defining the pathway of catalyst deactivation is a quite complex task since a multitude of carbon sources may be responsible for coke formation. Some reactions have been argued to play a part in the genesis of carbon deposition on catalyst surface. As examples, glycerol decomposition (Eq. (9)) [46], formation of glycerol oligomers [52,53] and production of coke precursors such as acetol, acrolein, acetaldehyde and ethylene [24,46,52] may be listed.

To further contribute to this discussion, the most deactivated catalyst ( $x=0$ ) was examined by TEM and representative images are illustrated in Fig. 9. Carbon deposits were invariably observed in the proximity of metal nanoparticles. It could be seen that Ni nanoparticles are confined into the internal nanostructure host (Fig. 9a) and eventually located at the ends of the carbon nanotubular structures. Along the examination of these samples it was also possible to identify carbon tubular nanostructures with an open end where it is suggested that Ni nanoparticles were detached (Fig. 9b). These findings suggest that Ni particles are intimately involved in the formation of those carbon filaments, most likely in the initiation step through a similar nucleation-growth mechanism well described for

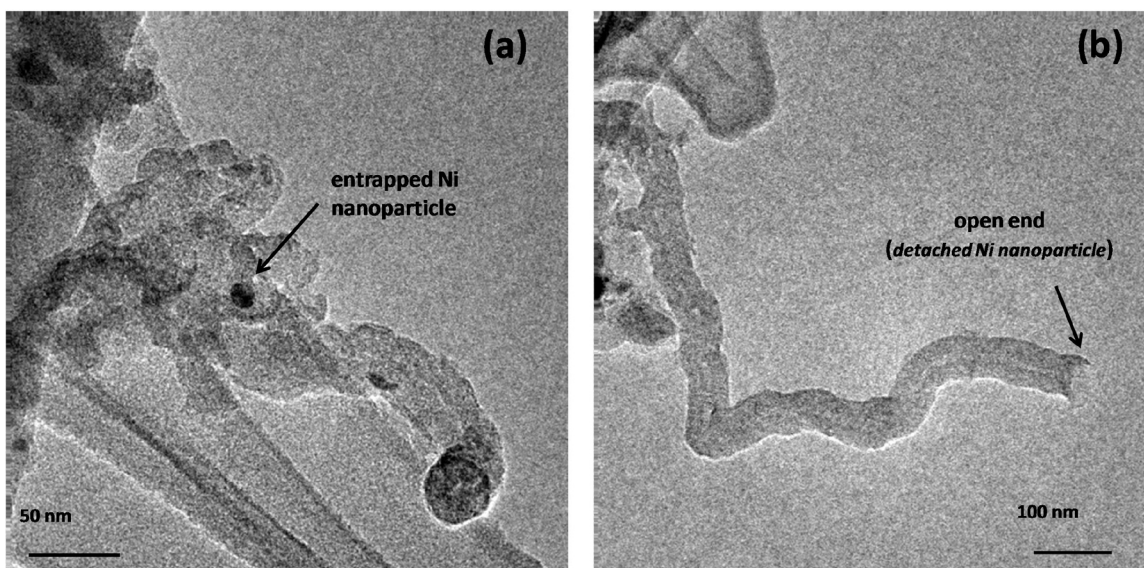


Fig. 9. Representative TEM images of metal supported catalysts derived from  $\text{LaNiO}_3$  ( $x=0$ ) after glycerol steam reforming.

hydrocarbon and alcohols reforming. The carbon species formed during the reaction may diffuse through the Ni crystallite and then nucleate and grow the carbon tubular nanostructures.

TPO/TGA analyses combined with mass spectrometry were complementarily performed for the used catalysts. The evolution of  $\text{CO}_2$  ( $m/z=44$ ) originated from the gasification of carbon deposits is depicted in Fig. 10. As different types of carbon species may be distinguished by their gasification temperature, it can be concluded that multiple carbon species are formed in different proportion over all samples. A first peak is observed at around  $360^\circ\text{C}$  being well or poorly defined according to the catalyst composition. Elimination

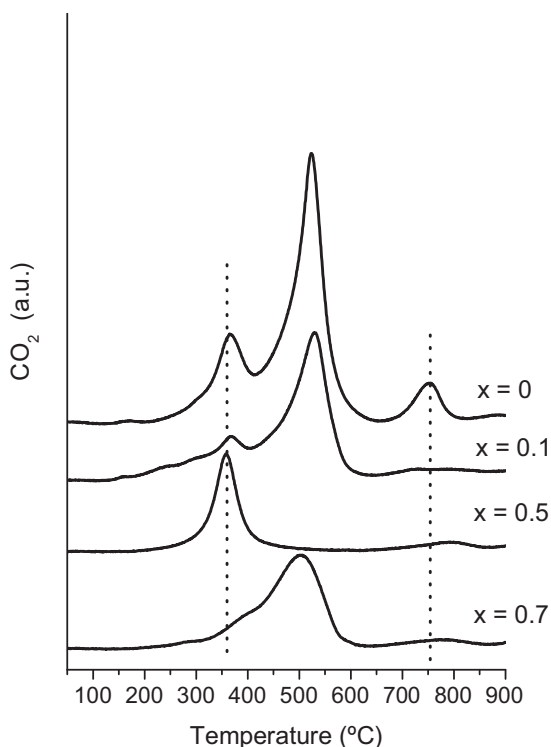


Fig. 10. Profiles of  $\text{CO}_2$  evolution obtained by TPO/TGA-MS analyses of all metal supported catalysts derived from  $\text{La}_{1-x}\text{Ce}_x\text{NiO}_3$  after glycerol steam reforming.

of carbon deposits in this temperature range is usually associated with highly reactive carbon species closer to the metal particles or amorphous carbon [34,51,52]. However, a minor water signal ( $m/z=18$ ) was also detected in the eluent gas phase composition, suggesting the existence of organic fragments on catalyst surface. Therefore both contributions should be considered to the formation of carbon residues gasified at such low temperatures.

A second component at  $500\text{--}530^\circ\text{C}$  is also present for all catalysts except for the one with 50% of La substitution by Ce ( $x=0.5$ ). Amongst those samples, the peak intensity noticeably decreases by increasing the amount of Ce. It is important to mention that  $\text{CO}_2$  was the only product identified within this temperature range and it is thus possible to assign this carbonaceous residue species to filamentous carbon [20,34,51]. The existence of carbon filaments was indeed verified during FE-SEM examination as presented hereinbefore (Figs. 8 and 9).

Finally, a third  $\text{CO}_2$  peak was registered at  $\sim 750^\circ\text{C}$  exclusively for the unsubstituted  $\text{LaNiO}_3$ -derived catalyst ( $x=0$ ). This type of carbonaceous deposit, which only generated  $\text{CO}_2$  in the gas phase, may be ascribed to more ordered graphitic carbon [34,52].

The TPO results markedly evidence the crucial role of La substitution by Ce in the mixed oxide catalyst precursor. Adding Ce dramatically improved the catalyst resistance to carbon deposition, determining both carbon type and quantity. The total amount of carbon species deposited onto each catalyst is summarized in Table 1. Degrees of substitution of 10% ( $x=0.1$ ) or 70% ( $x=0.7$ ) decreased, respectively, roughly twice or three times the amount of carbon per gram of catalyst (Table 1) and strongly hindered the formation of graphitic carbon. An optimal Ce loading, however, was accomplished at 50% since only a few amount of carbon was determined over  $\text{La}_{0.5}\text{Ce}_{0.5}\text{NiO}_3$ -derived sample ( $x=0.5$ ). Additionally, this substitution level allowed only the formation of the more reactive carbon species, whose gasification at low temperature is much easier. A satisfactory correlation between Ce content and carbon amount could indeed be reached as depicted in Fig. 11. This behaviour is likely bounded to the formation of  $\text{CeO}_2\text{--La}_2\text{O}_3$  solid solutions as evidenced by XRD, which may act as an oxygen buffer and therefore facilitate the removal of carbon deposits onto the catalyst surface. It is indeed well known that the improvement of oxygen storage capacity of lanthanides-doped fluorite  $\text{CeO}_2$  structure are noticeably affected by the composition [38,54]. The benefits of the formation of  $\text{CeO}_2$ -based solid solutions have been

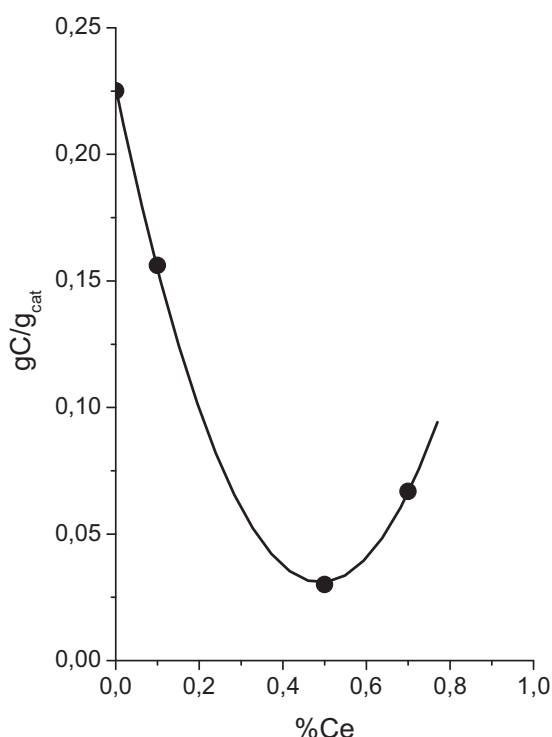


**Fig. 11.** Correlation between the amount of carbon deposited on the used catalysts (gC/g<sub>cat</sub>) and Ce content in the mixed oxide catalyst precursor.

reported for methane and ethanol reforming over the past years [34,55].

It is interesting to note, however, the distinct behaviour of  $\text{La}_{1-x}\text{Ce}_x\text{NiO}_3$ -derived catalysts over ethanol and glycerol reforming. As recently reported by de Lima et al. [34], the catalyst with only 5% of Ce in the perovskite structure leads to the best catalytic performance with an outstanding resistance to deactivation on ethanol reforming. Our results indicate that a much higher amount of Ce (ten times higher) is required to bring up any benefit to catalyst stability on glycerol reforming. Glycerol is a highly functionalized and reactive molecule since it bears three hydroxyl groups – two bonded to primary carbon atoms and one attached to a secondary carbon – and thus it is quite conceivable that a rather different mechanism takes place when this polyol is used as feedstock. The expected stronger dissociative adsorption of glycerol would facilitate decomposition reaction (Eq. (9)) easily leading to a stronger carbon deposition [46]. The amounts of carbon deposits summarized in Table 1 match those recently reported elsewhere [20,24,46,51,52] but are significantly higher than those usually reported for ethanol reforming [34].

It is lastly important to underline the relevance of understanding the glycerol steam reforming reaction since it should contribute to the development of innovative reforming processes to generate green hydrogen from a wide range of more complex oxygen-bearing molecules derived from biomass.

#### 4. Conclusion

$\text{La}_{1-x}\text{Ce}_x\text{NiO}_3$  mixed oxides precursors originate active catalysts for glycerol steam reforming, producing hydrogen-rich gas stream. Deactivation occurs irrespective of catalyst composition; however, sample with 50% La substitution by Ce shows more resistance to deactivation comparing to other loadings. This sample possesses the lower amount of more reactive carbon deposits as revealed by TPO/TGA-MS. The minimization of the deactivation process in

glycerol reforming requires higher Ce contents and it is suggested to be associated with the formation of  $\text{CeO}_2$ – $\text{La}_2\text{O}_3$  solid solutions.

#### Acknowledgements

PROSUL/CNPq 490187/2010-2 (Brazil) and Fondecyt 1130005 (Chile) are acknowledged for financial support and fellowships. The authors thank Ms. Nataly Amorim from CETENE (Brazil) for TEM analyses. Zeiss is also acknowledged for providing the Axion Vision software.

#### References

- [1] V. Galvita, K. Sundmacher, *Appl. Catal. A: Gen.* 289 (2005) 121–127.
- [2] P. Ramirez de la Piscina, N. Homs, *Chem. Soc. Rev.* 37 (2008) 2459–2476.
- [3] L.V. Mattos, G. Jacobs, B. Davis, F.B. Noronha, *Chem. Rev.* 112 (2012) 4094–4123.
- [4] R.D. Cortright, R.R. Davda, J.A. Dumesic, *Nature* 418 (2002) 964–967.
- [5] G.W. Huber, J.W. Shabaker, J.A. Dumesic, *Science* 300 (2003) 2075–2077.
- [6] R.R. Soares, D.A. Simonetti, J.A. Dumesic, *Angew. Chem. Int. Ed.* 45 (2006) 3982–3985.
- [7] A.O. Menezes, M.T. Rodrigues, A. Zimmaro, L.E.P. Borges, M.A. Fraga, *Renew. Energy* 36 (2011) 595–599.
- [8] D.A. Simonetti, E.L. Kunkes, J.A. Dumesic, *J. Catal.* 247 (2007) 298–306.
- [9] S. Adhikari, S. Fernando, A. Haryanto, *Energy Fuels* 21 (2007) 2306–2310.
- [10] A.M.D. Douette, S.Q. Turn, W. Wang, V.I. Keffer, *Energy Fuels* 21 (2007) 3499–3504.
- [11] M.L. Dieuzeide, V. Iannibelli, M. Jobbagy, N. Amadeo, *Int. J. Hydrogen Energy* 37 (2012) 14926–14930.
- [12] Y. Cui, V. Galvita, L. Rihko-Struckmann, H. Lorenz, K. Sundmacher, *Appl. Catal. B: Environ.* 90 (2009) 29–37.
- [13] N. Luo, X. Fu, F. Chao, T. Xiao, P.P. Edwards, *Fuel* 87 (2008) 3483–3489.
- [14] M. Slinn, K. Kendall, C. Mallon, J. Andrews, *Bioresour. Technol.* 99 (2008) 5851–5858.
- [15] T. Hirai, N.O. Ikenaga, T. Miyake, T. Suzuki, *Energy Fuels* 19 (2005) 1761–1762.
- [16] P.J. Dauenhauer, J.R. Salge, L.D. Schmidt, *J. Catal.* 244 (2006) 238–247.
- [17] V. Chiodo, S. Freni, A. Galvagno, N. Mondello, F. Frusteri, *Appl. Catal. A: Gen.* 381 (2010) 1–7.
- [18] B. Zhang, X. Tang, Y. Li, Y. Xu, W. Shen, *Int. J. Hydrogen Energy* 32 (2007) 2367–2373.
- [19] A. Iriondo, M.B. Guemez, V.L. Barrio, J.F. Cambra, P.L. Arias, M.C. Sanchez-Sanchez, R.M. Navarro, J.L.G. Fierro, *Scientific Bases for the Preparation of Heterogeneous Catalysts*, vol. 175, Elsevier, Amsterdam, 2010, pp. 449–452.
- [20] M.L. Dieuzeide, M. Jobbagy, N. Amadeo, *Catal. Today* (2013), <http://dx.doi.org/10.1016/j.cattod.2013.02.015>.
- [21] J.W. Shabaker, G.W. Huber, J.A. Dumesic, *J. Catal.* 222 (2004) 180–191.
- [22] J.W. Shabaker, D.A. Simonetti, R.D. Cortright, J.A. Dumesic, *J. Catal.* 231 (2005) 67–76.
- [23] A. Iriondo, V.L. Barrio, J.F. Cambra, P.L. Arias, M.B. Güemez, R.M. Navarro, M.C. Sanchez-Sanchez, J.L.G. Fierro, *Catal. Commun.* 10 (2009) 1275–1278.
- [24] I.N. Buffoni, F. Pompeo, G.F. Santori, N.N. Nichio, *Catal. Commun.* 10 (2009) 1656–1660.
- [25] B.L. Augusto, L.O.O. Costa, F.B. Noronha, R.C. Colman, L.V. Mattos, *Int. J. Hydrogen Energy* 37 (2012) 12258–12270.
- [26] J.R. Rostrup-Nielsen, J. Sehested, J. Norskov, *Adv. Catal.* 47 (2002) 65–139.
- [27] V.R. Choudhary, B.S. Uphade, A.A. Belhekar, *J. Catal.* 163 (1996) 312–318.
- [28] M.R. Goldwasser, M.E. Rivas, E. Pietri, M.J. Pérez-Zurita, M.L. Cubeiro, L. Gíngembre, L. Leclercq, G. Leclercq, *Appl. Catal. A: Gen.* 255 (2003) 45–57.
- [29] M.R. Goldwasser, M.E. Rivas, E. Pietri, M.J. Pérez-Zurita, M.L. Cubeiro, A. Grivobal-Constant, G. Leclercq, *J. Mol. Catal. A: Chem.* 228 (2005) 325–331.
- [30] G. Valderrama, M.R. Goldwasser, C.U. de Navarro, J.M. Tatibouët, J. Barrault, C. Batiot-Dupeyrat, F. Martínez, *Catal. Today* 107 (2005) 785–791.
- [31] M.A. Pena, J.L.G. Fierro, *Chem. Rev.* 101 (2001) 1981–2017.
- [32] S.M. Lima, J.M. Assaf, M.A. Peña, J.L.G. Fierro, *Appl. Catal. A: Gen.* 311 (2006) 94–104.
- [33] S.M. de Lima, A.M. da Silva, L.O.O. da Costa, J.M. Assaf, G. Jacobs, B.H. Davis, L.V. Mattos, F.B. Noronha, *Appl. Catal. A: Gen.* 377 (2010) 181–190.
- [34] S.M. de Lima, A.M. da Silva, L.O.O. da Costa, J.M. Assaf, L.V. Mattos, R. Sarkari, A. Venugopal, F.B. Noronha, *Appl. Catal. B: Environ.* 121/122 (2012) 1–9.
- [35] L.A. Chick, L.R. Pederson, G.D. Maupin, J.L. Bates, *Mater. Lett.* 10 (1990) 6–12.
- [36] G. Pecchi, P. Reyes, R. Zamora, L.E. Cadús, J.L.G. Fierro, *J. Solid State Chem.* 181 (2008) 905–912.
- [37] F.J. Perez-Alonso, I. Melian-Cabrera, M. Lopez Granados, F. Kapteijn, J.L.G. Fierro, *J. Catal.* 239 (2006) 340–346.
- [38] A.M. Duarte de Farias, D. Nguyen-Thanh, M.A. Fraga, *Appl. Catal. B: Environ.* 93 (2010) 250–258.
- [39] J.E. Spanier, R.D. Robinson, F. Zhang, S.-W. Chan, I.P. Herman, *Phys. Rev. B* 64 (2001) 245407–1–245407–8.
- [40] A. Bueno-Lopez, K. Krishna, M. Makkee, J.A. Moulijn, *J. Catal.* 230 (2005) 237–248.
- [41] C. Batiot-Dupeyrat, G. Valderrama, A. Meneses, F. Martinez, J. Barrault, J.M. Tatibouët, *Appl. Catal. A: Gen.* 248 (2003) 143–151.

- [42] H. Provendier, C. Petit, C. Estournes, S. Libs, A. Kienemann, *Appl. Catal. A: Gen.* 180 (1999) 163–173.
- [43] H. Falcon, E.E. Carbonio, J.L.G. Fierro, *J. Catal.* 203 (2001) 264–272.
- [44] G. Sierra, F. Mondragón, J. Barrault, C. Batiot-Dupeyrat, *Catal. Today* 133–135 (2008) 200–209.
- [45] C.K. Cheng, S.Y. Foo, A.A. Adesina, *Catal. Commun.* 12 (2010) 292–298.
- [46] C.K. Cheng, S.Y. Foo, A.A. Adesina, *Catal. Today* 164 (2011) 268–274.
- [47] D.L. Trimm, *Catal. Today* 37 (1997) 233–238.
- [48] D.L. Trimm, *Catal. Today* 49 (1999) 49–56.
- [49] N. Jeong, J. Lee, *J. Catal.* 260 (2008) 217–226.
- [50] A.L.M. da Silva, L.V. Mattos, J.P. den Breejen, J.H. Bitter, K.P. de Jong, F.B. Noronha, *Catal. Today* 164 (2010) 262–267.
- [51] F. Pompeo, G.F. Santori, N.N. Nichio, *Catal. Today* 172 (2011) 183–188.
- [52] L.F. Bobadilla, A. Álvarez, M.I. Domínguez, F. Romero-Sarria, M.A. Centeno, M. Montes, J.A. Odriozola, *Appl. Catal. B: Environ.* 123/124 (2012) 379–390.
- [53] J. Barrault, J.-M. Clacens, Y. Pouilloux, *Top. Catal.* 27 (2004) 137–142.
- [54] S. Letichevsky, M.A. Fraga, R.R. Avillez, C.A. Tellez, M.I.P. Silva, L.G. Appel, *Appl. Catal. B: Environ.* 58 (2005) 203–210.
- [55] S. Stagg, F.B. Noronha, E.C. Fendley, D.E. Resasco, *J. Catal.* 194 (2000) 240–249.